GPS Solutions (2026) 30:101
https://doi.org/10.1007/s10291-026-02064-2

RESEARCH

Precise time transfer and ranging for next-generation GNSS

Janis Surof[1,2] · Juraj Poliak[1] · Raphael Wolf[1] · Ramon Mata Calvo[1,3] · Ludwig Blümel[1] · Christoph Günther[2]

Received: 22 August 2025 / Accepted: 7 March 2026 / Published online: 25 March 2026

Abstract

Global navigation satellite systems broadcast signals for positioning estimation and time dissemination to end users. Current systems rely on ground-based observations and predictions. The Kepler system deviates from that by employing bidirectional optical inter-satellite links for time synchronization and orbit determination. This approach increases resilience, reduces ground infrastructure requirements and improves end-user accuracy. Optical two-way time transfer at sub-picosecond level and ranging at sub-millimeter precision are achieved by means of a chip rate of 12.8 Gcps and high-resolution optical correlation tracking. Our laboratory demonstrator verifies this concept. Two-way optical time transfer with a short-term stability below $1.8 \cdot 10^{-13}$ was demonstrated over a 30 m free space range. The received optical signal power was scaled to emulate a medium earth orbit inter-satellite distance of over 50,000 km. The hardware is rather similar to the one used in coherent optical communications systems and thus of limited complexity. This confirms that a system architecture based on bidirectional optical free-space links can achieve the required precision in time synchronization and orbit estimation in future global navigation satellite systems.

Keywords GNSS · Two-way time transfer · Ranging · Coherent communications · Optical inter-satellite link

Introduction

Our society is highly dependent on positioning and time synchronization through Global Navigation Satellite Systems (GNSS). The orbits and clock offsets of GNSS satellites are tracked using a large number of ground stations. Civil and scientific applications require ever greater precision and accuracy down to sub-centimeter and picosecond-levels. Radio Frequency (RF) inter-satellite links, such as those implemented in Beidou, were mainly foreseen for data distribution but can also be used for satellite clock offset and distance estimation with an approximated accuracy of 10 cm (Zhou et al. 2018). A novel GNSS architecture based on Optical Inter-Satellite Links (OISL), called Kepler, was proposed in (Günther 2018a). A system concept that accelerates the implementation is described in (Günther 2018b). A general overview of the utilized technologies is given in (Giorgi et al. 2019). OISLs enable synchronization, inter-satellite ranging and communications. The synchronization reaches picosecond level by means of optical two-way time transfer (TWTT). The OISLs furthermore estimate the distances between satellites with sub-millimeter precision to support precise orbit determination. Lastly, a data channel disseminates the determined measurement results and estimates, and thus enables a resilient constellation network. As a consequence, such a system operates with a high level of autonomy in space and does not rely on a complex ground system for orbit and clock offset determination or data distribution. Theoretically, it requires only two ground stations to connect to the earth's reference and time frame. With time synchronization at the picosecond level and ranging accuracy at the millimeter level, the Signal-in-Space Range Error (SiSRE) is significantly reduced as shown in (Michalak et al. 2021). This translates into both an improved positioning and synchronization of the end users, as well as into a faster convergence of precise point positioning.

✉ Janis Surof
Janis.Surof@dlr.de

[1] German Aerospace Center (DLR), Institute of Communications and Navigation, Münchener Strasse 20, 82234 Weßling, Germany

[2] Technical University of Munich, Arcisstrasse 21, 80333 Munich, Germany

[3] Present address: European Space Agency, Keplerlaan 1, 2201 AZ Noordwijk, The Netherlands

Optical transmission provides a significantly greater bandwidth than RF links, enabling a much higher precision. In addition, OISLs are inherently immune to interference, making the system robust against spoofing and jamming (Andrews and Phillips 2005). Free Space Optical (FSO) TWTT was demonstrated by (Giorgetta et al. 2013) over 2 km using optical frequency comb pulses. They reached a precision of $< 1 \cdot 10^{-15}$ at 1 s gate time. However, the use of optical clocks and frequency combs is associated with a high complexity. The comb pulses cover a broad spectrum that may not be compatible with currently available space terminals. Moreover, the Doppler shift between two Medium Earth Orbit (MEO) satellites in different orbital planes is challenging for such systems. The widely used White Rabbit protocol (Lipiński et al. 2011) is limited to static environments. Frame-based time synchronization applied in the *Optical Communications Terminal* standard of the *Space Development Agency* is expected to achieve time transfer with nanosecond accuracy (Wayne et al. 2024).

The system discussed in our paper modulates a spreading code onto an optical carrier at a high rate. The modulation format is Binary Phase Shift Keying (BPSK). The link budget required for pointing, acquisition and tracking is closed with 10 W transmit power and an aperture diameter of 80 mm over an inter-satellite distance of 50,000 km. The scenario is less demanding with respect to the modulation than for the European Data Relay System (EDRS) at a data rate of 1.8 Gbps (Hauschildt et al. 2019), since the effective data rate which determines the link budget is only 50 Mbps. EDRS has demonstrated successful data transmission over distances of up to 100,000 km (Heine et al. 2014).

The proposed technology leverages well-proven optical communications technologies with concepts from GNSS for time transfer and ranging. Most of the components are available in space-grade versions. This enables a fast development and application to future GNSS. The paper demonstrates the feasibility of precise time of arrival estimation using high-rate BPSK spreading sequences and optical correlation in a static environment. The latter correlation is key for achieving an high accuracy with a modest link budget. An analysis of the reception scheme and the control loops for code tracking and for carrier tracking is performed. The laboratory demonstrator used for system verification is described. The results of the TWTT experiments are presented.

System

The bidirectional OISL system between Satellites A and B is shown in Fig. 1. Both satellites have the same functional capabilities. The transceivers are referenced to the satellite clocks at the respective RFs f_A and f_B. All clocks are referenced to GNSS system time t. The clock offsets of the Transceivers A and B are δt_A and δt_B with respect to GNSS system time, respectively. The transceivers are capable of generating and detecting the fiber-coupled signals. They also handle the processing tasks necessary for time transfer and ranging. The OISL terminals couple the incoming free-space optical signal into an optical fiber by means of an active tip/tilt correction to compensate for residual satellite attitude errors and micro-vibrations. The terminals direct the transmission beam towards the remote terminal. The forward link (red - B → A) and return link (yellow - A → B) are generally operated at different wavelengths and/or polarization. The transceivers are wavelength agnostic, and thus do not pose any constraint on the beam separation strategy

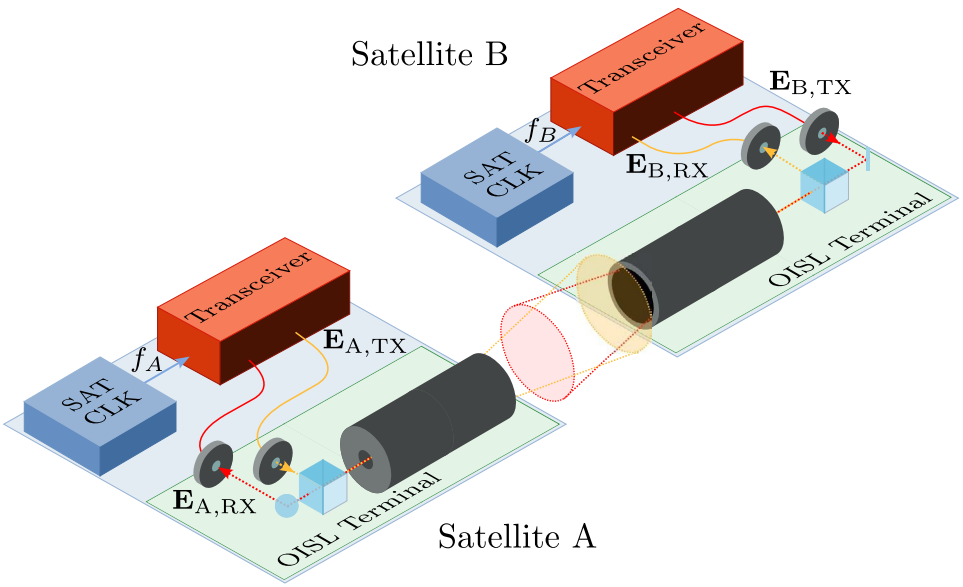

Fig. 1 Bidirectional transmission system (solid line - fiber-coupled, dotted - Free space and Optical Inter-Satellite Link (OISL), yellow - A → B, red - B → A) for time transfer, ranging and communications between two satellites with frequency references f_A and f_B from the satellite clocks (SAT CLK) (blue)

in the optical terminals. The description of the OISL terminals has been simplified to focus on the transceiver functionalities. A detailed description of the terminals is found in (Poliak et al. 2018).

The transceiver of one satellite is illustrated in Fig. 2. The optical transmission path is yellow, while the reception path is marked in red. RF signal propagation paths are blue. The process of generating the spread-spectrum sequences is illustrated in green. The sequences on the transmitter and receiver side are synchronized to the internal clock.

The transmitted signal is generated by digitally multiplexing the data signal b_{TX} with the Pseudo Random Noise (PRN) spreading sequence c_{TX}. The resulting sequence is modulated onto the optical carrier using a Mach–Zehnder modulator. The modulator converts the electrical signal into a phase modulation of the optical carrier, leading to the transmitted optical signal $\mathbf{E}_{\mathrm{TX}}$. The signal is received by the other satellite as $\mathbf{E}_{\mathrm{RX}}(t)$ (see Fig. 1).

The receiver system description is based on the forward link connecting Transmitter B to Receiver A. The received signal $\mathbf{E}_{\mathrm{RX}}$ is attenuated by the combined loss mainly due to propagation and fiber coupling. It is shifted by the propagation time Δt and has an offset δt_B with respect to GNSS system time. The received signal is thus given by

$$\begin{aligned}\mathbf{E}_{\mathrm{RX}}(t,\Delta t) =& \sqrt{P_{\mathrm{RX}}} b_{\mathrm{RX}}(t) c_{\mathrm{RX}}(t) \\ & \cdot \exp\left\{ j\left[2\pi f_c (t-\Delta t) \right.\right. \\ & \left.\left. + \phi_{\mathrm{c}}(t-\Delta t)\right]\right\},\end{aligned} \tag{1}$$

where P_{RX} is the received optical power, $b_{\mathrm{RX}}(t) = b(t+\delta t_B - \Delta t)$ is the data signal, $c_{\mathrm{RX}}(t) = c(t+\delta t_B - \Delta t)$ is the spreading sequence and f_c is the optical carrier frequency. The carrier phase noise $\phi_c(t)$ associated with FSO links is discussed in (Surof et al. 2017). Note that in contrast to GNSS, f_c is not related to f_B and δt_B and hence carrier and code phase have to be addressed separately. Coherent detection for communications purposes is usually performed by mixing the incoming beam with an unmodulated optical Local Oscillator (LO). However, to enable optical correlation, the optical LO is modulated by the same PRN sequence that is used for transmission. It is expressed with $c_{\mathrm{LO}}(t) = c(t+\delta t_A)$. The optical LO signal is described by:

$$\mathbf{E}_{\mathrm{LO}}(t) = \sqrt{P_{\mathrm{LO}}} c_{\mathrm{LO}}(t) \exp\left\{ j\left[2\pi f_{\mathrm{LO}} t + \phi_{\mathrm{LO}}(t)\right]\right\}. \tag{2}$$

In this equation P_{LO} denotes the optical power of the LO, f_{LO} its frequency, and $\phi_{\mathrm{LO}}(t)$ its phase noise, including an arbitrary initial phase shift relative to $\phi_{\mathrm{c}}(t)$. The optical mixing is performed in an optical 90° hybrid, as shown in Fig. 2. Four optical splitters and a 90° phase delay combine the signals to generate four output signals $\mathbf{E}_{I1}$, $\mathbf{E}_{I2}$, $\mathbf{E}_{Q1}$ and $\mathbf{E}_{Q2}$ with relative phases of 0°, 180°, 90°, 270°, respectively (see e.g. Seimetz (2009)). The optical power of $\mathbf{E}_{I1} = \frac{1}{2}\left(-j\mathbf{E}_{\mathrm{RX}} - j\mathbf{E}_{\mathrm{LO}}\right)$

$$P_{\mathrm{I1}}(t,\Delta t) = \frac{1}{4}(-j\mathbf{E}_{\mathrm{RX}} - j\mathbf{E}_{\mathrm{LO}})(j\mathbf{E}^*_{\mathrm{RX}} + j\mathbf{E}^*_{\mathrm{LO}}) \tag{3}$$

is detected by a photo diode. P_{I1} is expanded into

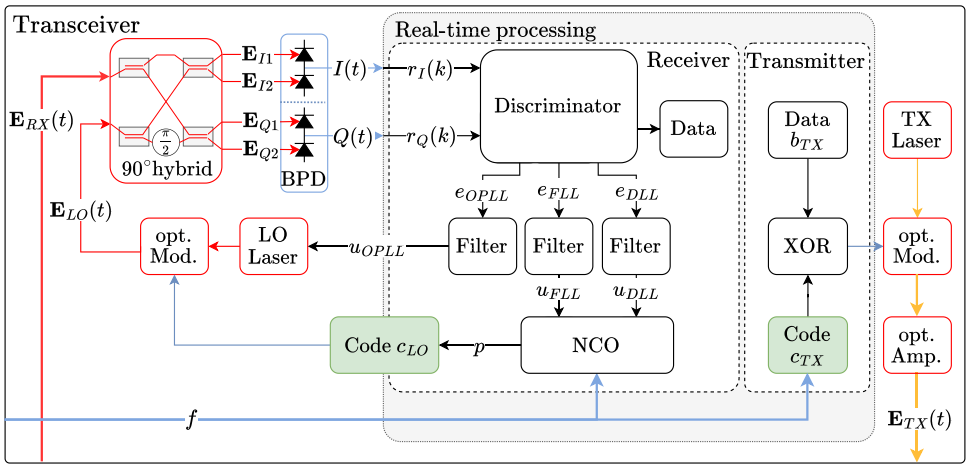

Fig. 2 The transceiver includes a coherent receiver with 90° hybrid and Balanced Photo Detectors (BPD) generating in-phase and quadrature signals for signal processing using phase discrimination and loop filtering for Optical Phase Locked Loop (OPLL) to steer the optical Local Oscillator (LO) laser. For code tracking, a Frequency and Delay Locked Loop (FLL, DLL) with Numerical Controlled Oscillator (NCO) control the local reference code modulation c_{LO}. The transmitter multiplexes (XOR) the data signal with the spreading code and modulates it onto the transmitter (TX) laser. The signal is optically amplified (opt. Amp.) and transmitted. The real-time processing unit derives its clock from an external reference with frequency f

$$P_{\mathrm{I1}}(t,\Delta t) = \frac{1}{4}\Big\{ P_{\mathrm{RX}} + P_{\mathrm{LO}} + 2\sqrt{P_{\mathrm{RX}}P_{\mathrm{LO}}}\, b_{\mathrm{RX}}(t)c_{\mathrm{RX}}(t)c_{\mathrm{LO}}(t) \cdot \cos\left[2\pi(f_{\mathrm{off}}t - f_c\Delta t) + \phi_n(t)\right]\Big\}, \tag{4}$$

with the optical carrier frequency offset $f_{\mathrm{off}} = f_c - f_{\mathrm{LO}}$ and a combined phase noise term $\phi_n(t) = \phi_{\mathrm{c}}(t+\Delta t) - \phi_{\mathrm{LO}}(t)$. This representation emphasizes that the multiplication of the correlation between $c_{\mathrm{RX}}(t)$ and $c_{\mathrm{LO}}(t)$ is carried out in the optical domain. As a consequence, detection and sampling are performed at a much lower sampling rate than the spreading sequence.

The remaining three optical signals P_{I2}, P_{Q1}, P_{Q2} are derived similarly. The signals are converted in the electrical domain by photo diodes. The in-phase and quadrature components of the received signal are recovered, by subtracting the respective photocurrent pairs i_{I1}, i_{I2} and i_{Q1}, i_{Q2} in balanced photo detectors. In the following, the recovery of the in-phase is derived. The quadrature phase is obtained analogously. The in-phase signal is described by

$$I(t,\Delta t) = i_{I1} - i_{I2} = A_R\big[P_{I1}(t,\Delta t) - P_{I2}(t,\Delta t)\big] + n_{\mathrm{s}}(t), \tag{5}$$

where A_R is the responsivity of the photo diodes and $n_s(t)$ is the shot-noise. The noise variance is given by $\sigma_s^2 = qA_RP_{\mathrm{LO}}\Delta f$ (Agrawal 2010) with the elementary charge of an electron q and the bandwidth of the receiver circuit Δf. Usually P_{LO} is much larger than P_{RX} and therefore the shot-noise term dominates the additive noise terms (Agrawal 2010). The signal is integrated and digitized at the sampling rate T_s. The data rate and T_s are related by the Nyquist criterion. The kth sample of the digitized signal is given by

$$r_{\mathrm{I}}(k,\Delta t) = \frac{A}{T_s}\int_{(k-\frac{1}{2})T_s}^{(k+\frac{1}{2})T_s} b_{\mathrm{RX}}(t)c_{\mathrm{RX}}(t)c_{\mathrm{LO}}(t) \cdot \cos\left[2\pi(f_{\mathrm{off}}t - f_c\Delta t) + \phi_n(t)\right]dt + n_i(k), \tag{6}$$

with $A = A_R\sqrt{P_{\mathrm{RX}}P_{\mathrm{LO}}}$. The variance of the noise n_{i} is described by $\sigma_i^2 = \frac{\sigma_s^2}{T_s}$ for uncorrelated noise. When f_{off} is large, r_{I} will average to 0. Therefore, the frequency offset f_{off} has to remain inside the intradyne window for BPSK ($f_{\mathrm{off}} < |\frac{1}{4T_s}|$) (Seimetz 2009). In this case, r_{I} is approximated by

$$r_{\mathrm{I}}(k,\Delta t) \approx A\, b(k)R(\tau) \cdot \cos\left[2\pi(f_{\mathrm{off}}kT_s - f_c\Delta t) + \phi_n(kT_s)\right] + n_{\mathrm{i}}(k), \tag{7}$$

with the autocorrelation function

$$R(\tau) = \int_{(k-\frac{1}{2})T_s+\delta t_A}^{(k+\frac{1}{2})T_s+\delta t_A} c(t+\tau)c(t)dt. \tag{8}$$

The clock offsets and the propagation time are combined to $\tau = \delta t_B - \delta t_A - \Delta t$. For a Maximum Length Shift Register (MLSR) sequence, $R(\tau)$ has the form:

$$R(\tau) = \begin{cases} 1 - \frac{|\tau|}{T_c}, & \text{for} \quad |\tau| \le T_c \\ -\frac{T_c}{T_s}, & \text{elsewhere,} \end{cases} \tag{9}$$

with the chip length T_c. The samples of the quadrature signal are obtained in a similar way:

$$r_{\mathrm{Q}}(k,\tau) \approx A\, b(k)R(\tau) \cdot \sin\left[2\pi(f_{\mathrm{off}}T_sk - f_c\Delta t) + \phi_n(k)\right] + n_{\mathrm{q}}(k). \tag{10}$$

Equations (7) and (10) are composed of three major elements - the transmitted data $b(k)$, the code correlation term $R(\tau)$ and a carrier phase term with the argument $2\pi(f_{\mathrm{off}}T_sk - f_c\Delta t) + \phi_n(k)$. The combination of $\delta t_B - \delta t_A - \Delta t$ is exposed by $R(\tau)$ and tracked in the Delay Locked Loop (DLL). As the code phase and optical phase are independent, the optical carrier phase term is controlled in an Optical Phase Locked Loop (OPLL). Additionally, there are shot-noise terms in the in-phase and quadrature component. The two noise terms n_{i} and n_{q} are independent and have the same variance. As long as $R(\tau)$ is not tracked, the carrier term cannot be evaluated. On the other hand, the receiver structure cannot receive a signal when f_{off} is too large. An acquisition procedure is necessary to establish the interdependent code and carrier tracking.

The process to lock both loops is presented in Fig. 3. After physical link acquisition at t_1, an unmodulated carrier is transmitted to determine f_{off}. The Doppler shift resulting from $f_c\Delta t$, if the satellites are in relative motion, is compensated in open-loop with a priori orbit information. An accuracy of up to 100 m is sufficient and required anyway for physical link acquisition. At t_2, carrier and optical LO are aligned such that the PRN transmission can be activated. The Frequency Locked Loop (FLL) compensates for the code Doppler in open-loop mode. Simultaneously, the DLL initiates a search over the PRN sequence. When the peak is found at t_3, the DLL starts tracking and the FLL in the code

Time	Carrier			Code		
	alignment	OPLL	f_{off}, Φ_n	FLL	DLL	τ
t_1		open	$f_{\text{off}} < \frac{1}{4T_s}$	no modulation		unkown
t_2	Doppler prediction			PRN modulation: Doppler prediction	PRN scan	$< T_c$
t_3						
t_4	OPLL unload	locked	$f_{\text{off}} = 0$ $\Phi_n = 0$	locked	locked	0

Fig. 3 Sequential acquisition procedure for carrier and code locking tracking

domain is locked. At t_4 the OPLL is locked and the data transfer is enabled.

The coherent code discriminator of Eqs. (7) and (10) is still modulated by the data bits $b(k)$. Taking the power $|r(k,\tau)|^2$ removes the data $b(k)$ and any residual carrier phase offset. The code tracking uses the resulting power measurement over one or several integration intervals:

$$\begin{aligned} S(i,\tau) &= \frac{1}{N} \sum_{k=(i-1)N+1}^{iN} \left[r_I^2(k,\tau) + r_Q^2(k,\tau)\right] \\ &\approx A^2 R^2(\tau) + n_{\text{I}}^2(k) + n_{\text{Q}}^2(k), \end{aligned} \tag{11}$$

where N denotes the number of samples and $i = N \cdot k$ the sample index of $S(i,\tau)$. The noise variances are given by $\sigma_I^2 = \sigma_Q^2 = \frac{\sigma_i^2}{N}$. The resulting signal $S(\tau)$ is neither dependent on the data signal nor on the residual carrier offset. This is the basis for intradyne and homodyne detection. For the acquisition phase, the intradyne scheme is applied. The carrier phase term of Eqs. (7) and (10) is only coarsely controlled but still allows to evaluate Eq. (11). In homodyne reception the optical phase term argument is controlled to 0 and thus maximizes the power into $r_I(k,\Delta t)$. Applying both schemes allows for the effective implementation of the presented code and carrier phase lock acquisition algorithm from Fig. 3.

During the acquisition process, τ is determined by scanning $c_{\text{LO}}(t)$ in steps of a half a chip length until the correlation is detected. Once found, the code phase is tracked. In RF systems it is common to correlate the sampled incoming signal with spreading sequences in an Early-Prompt-Late (EPL) scheme (Kaplan and Hegarty 2005). Presently, the incoming signal is correlated in the optical and analog domain. Thus a corresponding split of the analog signal would result in a loss of power. In addition, the fiber lengths would have to be carefully matched to align the incoming signals with the delayed optical LO signals. To overcome this, $c_{\text{LO}}(t)$ is shifted back and forth in time on the same hardware in consecutive intervals. The phasing of the correlation is estimated by evaluating the power-scaled discriminator

$$e_{\text{DLL}}(m,\tau) = \frac{C_e(m,\tau) - C_l(m,\tau)}{C_p(m,\tau) - C_e(m,\tau) - C_l(m,\tau)}, \tag{12}$$

where $m = 4 \cdot i$ denotes the sample index of $e_{\text{DLL}}(m,\tau)$. The correlation values C_e, C_p and C_l, shifted to early, prompt and late, respectively, are obtained consecutively from

$$C_e(m,\tau) = S(4i-3,\tau) \tag{13}$$

$$C_p(m,\tau) = S(4i,\tau) + S(4i-2,\tau) \tag{14}$$

$$C_l(m,\tau) = S(4i-1,\tau). \tag{15}$$

The error e_{DLL} is filtered with a Proportional-Integral-Derivative (PID) controller for robust tracking of clock jitter and residual Doppler error. The resulting control signals u_{DLL} and u_{FLL} are applied to steer $c_{\text{LO}}(t) = c(t + \delta t_A + u_{\text{DLL}} + u_{\text{FLL}}t)$ in Eq. (2). When the correlation peak of $R(\tau)$ is successfully tracked, the steering signal follows

$$p_A = u_{\text{DLL}} = -\tau = \Delta t + \delta t_A - \delta t_B. \tag{16}$$

The steering signal p_A thus represents a combination of the clock offsets and of the propagation time from one satellite to the other one, which is actually the pseudorange. Delays caused by the hardware and environmental changes were not addressed in the present analysis. The study concentrates on the verification of the precision of time transfer and ranging. Relativistic effects or biases are not considered in the laboratory verification, but are addressed further in (Trainotti et al. 2022).

After establishing the DLL lock, the residual phase between the carrier and the optical LO is controlled by the OPLL. The phase error e_{OPLL} of a Costas loop (Costas 1956) discriminator for small $\phi_n(k)$ is given by

$$e_{\text{OPLL}} = r_{\text{I}}(k) \cdot r_{\text{Q}}(k) \approx 2\phi_n(k). \tag{17}$$

The loop filter is again designed as a PID controller. The proportional and derivative parts are used to compensate for phase noise ϕ_n. Residual frequency drifts are controlled by the integral part. The outer frequency alignment monitors u_{OPLL} to keep the OPLL within its operating range.

When the OPLL and DLL are locked, the data signal $b(k)$ is demodulated from Eq. (7). Data for time synchronization

and ranging, e.g. time stamps and pseudorange measurements from the remote terminal, are evaluated by the receiver. It was shown that the ranges can be used to estimate accurate orbits (Michalak et al. 2020). Similarly, the exchange of clock offsets was used to generate a composite system time and to thereby synchronize the clocks (Trainotti et al. 2022). This allows to form a resilient, robust and autonomous GNSS constellation by means of optical links.

Experimental evaluation

A laboratory demonstrator was built to verify the performance of the proposed system shown in Fig. 1. It comprised two elements, each containing a transceiver and an FSO terminal. The latter one is described in (Poliak et al. 2018). The units were placed at the two ends of a 30 m experimental range between laboratories A and B. The entire demonstrator consisted mostly of commercial off-the-shelf components. The exception was the electronic interface boards. The following section describes the implementation of the transceiver. Key parameters of the demonstrator are summarized in Table 1. The coarse alignment of the optical carrier frequency was performed by thermal tuning of the optical LO. The laser linewidth was selected to ensure an OPLL lock with the available optical LO bandwidth. Carrier tracking was implemented by piezo-tuning of the optical LO. When the piezo-tuning reached its limits, thermal adjustments were performed. The optical LO power at the entrance of the coherent receiver was 9.5 dBm. Therefore, the receiver was shot-noise limited. The link budget for pointing, acquisition and tracking was calculated for a MEO-MEO OISL over a distance of 50,000 km. The diameter of the optical terminals was set to 8 cm and a 10 W optical power amplifier was assumed. Based on the link budget analysis, the required receiver sensitivity was estimated at −57 dBm and used as the reference power level for laboratory verification. A pre-amplifier at the receiver was not required.

Digital signal processing for transmission and reception was implemented in a Field-Programmable Gate Array (FPGA) operated at a clock rate of 400 MHz which enabled real-time operation. The FPGA's clock was derived from a Dual Oven Controlled Oscillator (DOCXO) to emulate the local satellite clock or from an Active Hydrogen Maser (AHM) for system characterization purposes. A spreading sequence generated at a rate of 12.8 Gcps, i.e. $T_c = 78.13$ ps, was Manchester encoded using Binary Offset Carrier (BOC) modulation (Betz 2001). The FPGA's internal high-speed transceiver sampled the binary signal at 25.6 Gsps, that was then used to modulate the optical carrier. The sequence had a period of 256. It was obtained by appending a 0 to a MLSR sequence. This eased the implementation, at the price of a slightly degraded correlation performance. The rate of the user data was set to 50 Mbps. Each bit of b(k)

Table 1 Parameters of the laboratory demonstrator focusing on optical and radio frequency aspects

Parameter	Value	Unit	Note
Optical			
Wavelengths	1540/1564	nm	For forward/return link separation
Polarization	Circular	–	Forward–right hand/Return–left hand
LO thermal tuning range	15	GHz	Used for carrier alignment
Linewidth	< 1	kHz	Lorentzian
Optical LO bandwidth	100	kHz	Piezo-modulated, used for OPLL
Piezo tuning range	60	MHz	OPLL operation window
P_{LO}	9.5	dBm	Including modulator insertion loss
P_{RX}	−57	dBm	MEO-MEO OISL sensitivity
Radio frequency			
FPGA clock frequency	400	MHz	
DOCXO	$1 \cdot 10^{-13}$	–	Allan deviation at 1 s gate time
AHM	$1 \cdot 10^{-13}$	–	Allan deviation at 1 s gate time
PRN rate	12.8	Gcps	BOC(1,1), sampled at 25.6 Gsps
PRN length	256	chip	MLSR sequence with added 0
Data rate	50	Mbps	
Delay line interval	60	ps	$> \frac{T_c}{2} = 39.1$ ps
Delay modulation rate	400	MHz	Integer shift and delay line
Shift resolution	0.1	ps	
T_s	6.67	ns	
N	150	–	Integration time of 1 µs in Eq. (11)
Discriminator rate	250	kHz	E-P-L-P scheme applied
EPL spacingd_τ	$\frac{T_c}{10}$	s	≈ 8 ps

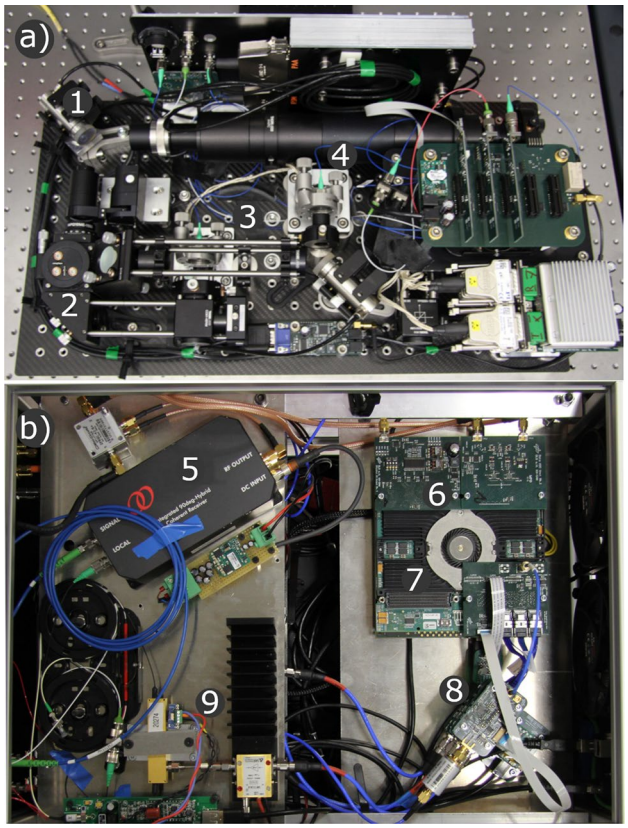

Fig. 4 **a** Optical terminal with fine steering mirror (1), beam separation (2), receiver (3) and transmitter fiber-coupling (5); **b** Transceiver with coherent receiver (5), receiver processing stage (6) with field programmable gate array (7), high speed sequence generation (8) and optical modulation stage (9)

was represented by a full period of a BOC(1,1) modulated spreading code.

The delayed replica c_{LO} of the spreading sequence, used to correlate the received signal, was generated in a combination of analog and digital processing steps. Shifts of $\frac{T_c}{2}$ were implemented in the digital domain. To increase the resolution for fine tracking and EPL modulation, an analog delay line was used for sub-chip shifts. The delay line shifted the analog signal in time according to an external steering signal, generated by the FPGA. The analog shift must cover at least the range of $[0, \frac{T_c}{2}]$ to allow the combination of digital and analog shifting. The delay was updated every 2.5 ns. The shifted reference PRN sequence was then modulated onto the optical LO to generate $\mathbf{E}_{\mathrm{LO}}(t)$ in Fig. 2.

The optical signals E_{RX} and E_{LO} were mixed in the 90° hybrid and detected by the low bandwidth photo diodes. The photo diodes reduced the bandwidth of the detected signals by an order of magnitude compared to the bandwidth of the spreading sequence. Subsequently, the bandwidth was further limited to approximately the Nyquist rate of the data rate, and the signals were sampled at a sampling period of $T_s = 6.67$ ns. This way approximations of r_I and r_Q cf. (7) and (10), respectively, were realized. A sequence of four delay stages—early, prompt, late, and prompt—was applied with an equal duration of 1 μs for each value, c.f. $N = 150$ in Eq. (11). This resulted in an error discriminator update rate of 250 kHz. A chip spacing $d_\tau = \frac{T_c}{10}$ was used for EPL shifting that related to around ± 4 ps shifts from prompt. This resulted in a power difference of 4% between prompt and shifts to early and late phasing, respectively.

The optical terminal is shown in Fig. 4a. The beam enters through the telescope and is reflected by a fine steering mirror (1). The transmitter and receiver signals are separated by wavelength and polarization at (2). The receiving beam is coupled into fiber at (3). The transmitting beam leaves the fiber at (4). The transceiver is shown in Fig. 4b. The coherent receiver (5) performs the optical correlation between the incoming signal and the local reference signal. The processing unit consists of analog to digital converters (6), an FPGA (7) and the PRN signal generators (8). The optical modulation of the LO laser is shown in (9). The transmitter modulation chain and the lasers are implemented beneath.

The system was verified in three steps. At first, the single direction B → A of the system was analyzed. This is represented in Fig. 5a via a 60 m optical fiber connection. The transmitter and receiver were referenced to the same AHM for common-mode operation.

This allowed for a characterization of the optical correlation without tracking loops. The reference signal $c_{\mathrm{LO}}(t)$ was shifted in steps of $\Delta\tau = 0.5$ ps over the correlation peak. The measurement points evaluating Eq. (11) are shown in Fig. 6 (yellow dots). The correlation peak with its side lobes is clearly visible. The measurements averaged over

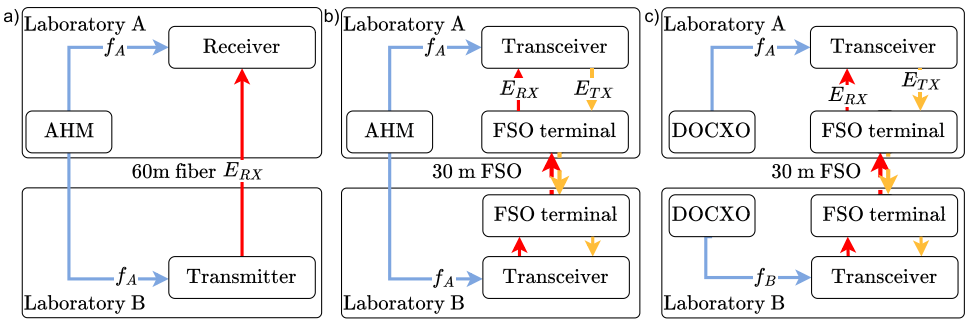

Fig. 5 **a** Common-mode fiber-coupled scenario for single link evaluation with an Active Hydrogen Maser (AHM); **b** Common-mode scenario over 30 m Free Space Optical (FSO) link; **c** Transmission over 30 m FSO with Dual Oven Controlled Oscillators (DOCXO) as references

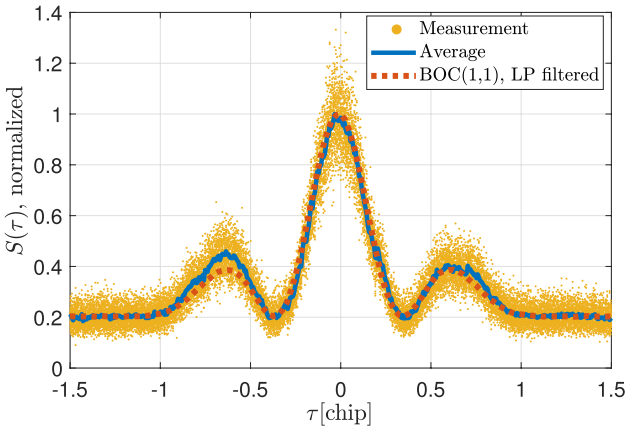

Fig. 6 Static non-coherent correlation peak measurement in 0.5 ps steps with the individual measurements (yellow dots), the averaged (blue line) and a comparison with a Low-Pass (LP) filtered binary offset carrier BOC(1,1) (red dashed) at 7 dB. All curves are normalized to the maximum averaged power value

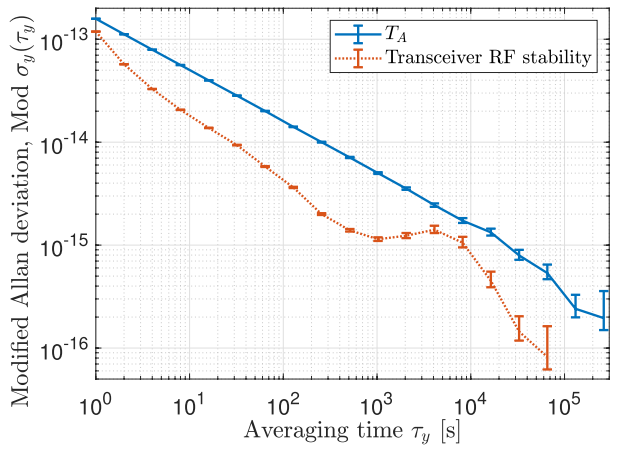

Fig. 7 Modified overlapping Allan deviation for unidirectional time transfer (blue line) over 16 days and corresponding Radio Frequency (RF) reference to Field Programmable Gate Array (FPGA) stability (red dotted) (Wolf et al. 2020)

a period of 1 μs are shown in blue. The noise floor stems from the non-coherent integration of the shot-noise terms cf. Eq. (11). The correlation peak was compared to a BOC(1,1) simulation that included shot-noise and low-pass filtered PRN signals with a cut-off of 19 GHz (red dashed). The bandwidth limitation is caused by the electrical signal paths from the FPGA to the optical modulators (see 7–9 in Fig. 4). The measurement and the simulation matched except for a small difference in the left side lobe. The side lobe deviation was caused from unequal rise and fall times during signal generation. A signal to noise ratio of 7 dB between the primary peak and the noise floor was estimated.

To verify the tracking loops of the system, the DLL and OPLL were run for 16 days. During the entire time, DLL and OPLL remained locked. The residual carrier phase had a standard deviation of $6°$ and an offset of $0.05°$. Only one single $180°$ phase slip of the OPLL was observed during the entire experiment, i.e. over a duration of more than 2 weeks. This demonstrates the excellent stability of the OPLL.

The modified Allan deviation Mod $\sigma_y(\tau_y)$ of the pseudorange p_A is shown in blue in Fig. 7. The error bars represent the statistical uncertainties of the calculation. It shows a stability of $1.6 \cdot 10^{-13}$ at 1 s averaging time. After 10^5 seconds the stability reached $3 \cdot 10^{-16}$. This result was compared to the electrical stability of a single transceiver RF chain. The corresponding experiment was reported by (Wolf et al. 2020). A 100 MHz RF signal generated by the transmitter was compared to the reference AHM in common-mode. The transceiver RF stability is shown in red in Fig. 7. The distortion at the 1000 s mark is due to the air-conditioning of the laboratory where the experiment was conducted. The optical transmission with a locked DLL has a comparable performance. Both DLL and OPLL demonstrated excellent phase stability and robustness over the 16 days period.

In the next step, the bidirectional system performance was evaluated over the 30 m FSO channel (Fig. 5b). Both FPGAs were still referenced to the same AHM for common-mode measurements. The bidirectional link over 30 m was established. OPLL and DLL were locked on both sides. To evaluate the performance of the system, the clock offset ΔT_{AB} and the propagation delay Δt between the transceivers were calculated. The clock offset ΔT_{AB} was estimated from the difference of the pseudoranges

$$\Delta T_{AB} = \frac{1}{2}\left(p_A - p_B\right) = +\delta t_A - \delta t_B. \tag{18}$$

with p_A from Eq. (16) and $p_B = \Delta t + \delta t_B - \delta t_A$ simultaneously measured at transceiver B. The sum provides the propagation delay and thus the distance between the terminals:

$$\Delta t = \frac{1}{2}\left(p_A + p_B\right). \tag{19}$$

The modified Allan deviation of ΔT_{AB} is shown in Fig. 8 (blue). This is the performance of the TWTT. It achieved a stability of $< 1.1 \cdot 10^{-13}$ at 1 s. The periodic switching of the air conditioning in Laboratory A induced a visible instability at around 100 s. The performance of the TWTT is comparable to the transceiver stability shown in Fig. 7. Neither the FSO terminals nor the tracking loops introduced a noticeable degradation.

Finally, individual DOCXOs were used as time references to emulate the real system, see Fig. 5c. The FLLs were pre-set with a constant rate to mitigate the drift between the DOCXOs. The modified Allan deviation of the TWTT with

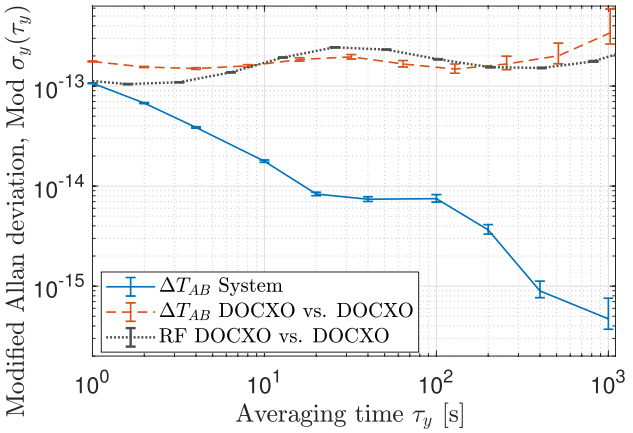

Fig. 8 Modified overlapping Allan deviation of two-way optical time transfer ΔT_{AB} over 30 m in common-mode using a single active hydrogen maser (AHM) (blue line), two-way optical time transfer (red dashed) over 30 m with dedicated dual oven controlled oscillators (DOCXO) and a radio frequency (RF) comparison of the DOCXOs for reference (grey dotted)

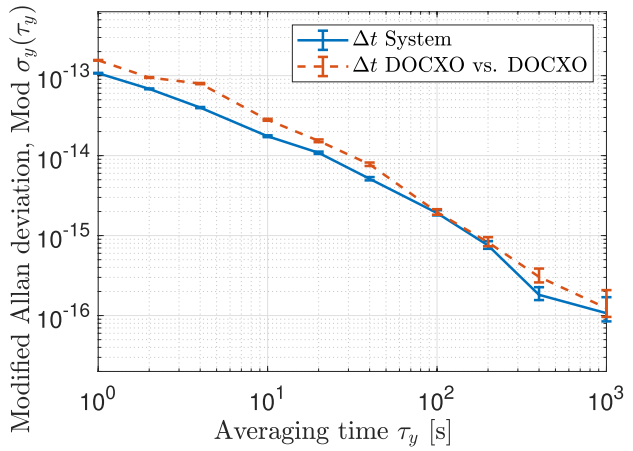

Fig. 9 Modified overlapping Allan deviation of the distance estimation Δt over 30 m in common-mode using a single active hydrogen maser (AHM) (blue line), Δt over 30 m with dedicated dual oven controlled oscillators (DOCXO) (red dashed)

DOCXOs (red dashed) is shown in Fig. 8. It achieves a short-term stability $< 1.8 \cdot 10^{-13}$. A direct RF comparison of the DOCXOs is plotted in dotted grey. The TWTT via the optical link and the direct lab comparison show a similar performance.

The ranging capabilities were verified by evaluation of the propagation time Δt. Note that the measurements are biased by hardware delays. Since those can be assumed to be constant during the measurements, they do not affect the stability analysis. The modified Allan Deviation for the common-mode scenario (see Fig. 5b) is shown in blue in Fig. 9. The curve shows a $1/\tau$ behavior. This was expected as the distance remained constant. As a consequence, the result was only affected by measurement noise. The stability of Δt with two DOCXOs (see Fig. 5b) is shown in dashed red in Fig. 9. It has a similar performance, since the clocks do not matter much in this setup. The stability is at $< 1.6 \cdot 10^{-13}$ at 1 s averaging time.

The TWTT and ranging precision at shorter time scales is evaluated using the standard deviation of the time series of Δt and ΔT_{AB}, respectively. For a time scale of 20 ms, which would allow for Doppler fitting, the standard deviation of TWTT is $\sigma_{\mathrm{TWTT}} = 0.37$ ps, and for ranging $\sigma_{\mathrm{range}} = 121$ μm. To further account for satellite vibrations, a read-out rate of 1 kHz is recommended. At a time scale of 1 ms the TWTT and ranging precision is extrapolated from the measured dataset to be around 2 ps and 600 μm, respectively. The target ranging precision enabled by optical links to achieve a significant reduction in SiSRE is at mm-level (Michalak et al. 2021). The performance is achieved at all studied time scales.

Conclusion

The TWTT method presented in this paper is able to synchronize two satellites with sub-picosecond precision by means of high-rate PRN sequences and optical correlation. The same setup also provides precise ranging. The system was verified with a laboratory demonstrator and showed a short-term system stability of $< 1.1 \cdot 10^{-13}$ for TWTT and ranging. A full system evaluation, including separate time references, achieved a time transfer precision better than < 0.4 ps and a ranging precision better than < 121 µmm at an averaging time of 20 ms in static conditions. The next phase will address the situation in the dynamic context. By extrapolation, we show that even for a time scale of 1 ms, picosecond-level time transfer and sub-millimeter ranging can be achieved. The results provide some margin for potential penalties, for example, resulting from micro-vibrations or residual Doppler offsets. At the same time, the complexity of the system is sufficiently low for the implementation in future GNSS. The successful long-term evaluation over more than 2 weeks showed the robustness of the implementation. The high receiver sensitivity allows for inter-satellite ranges up to 50,000 km using state-of-the-art optical terminals. A near-term implementation is possible due to the high technology readiness level. In-orbit validation shall be addressed soon.

Acknowledgements This project was supported by the Helmholtz-Gemeinschaft Deutscher Forschungszentren e.V. under grant numbers ZT-0007 (ADVANTAGE, Advanced Technologies for Navigation and Geodesy). The project ADVANTAGE was a joint project of DLR and the Geo Forschungszentrum (GFZ) Postdam. It aimed at defining a future system for navigation, geodesy and metrology.

Author Contributions All authors contributed to the study conception and design. C.G. proposed the optical correlation. J.S. designed the

transceiver system. Management and coordination responsibility for the research activity were performed by R.M.C and J.P.. The experiment realization and the data collection were performed by J.S., J.P., R.W., L.B. and R.M.C. The data analysis was performed by J.S. and L.B.. The software and firmware used was developed by R.W. and J.S.. The first draft of the manuscript was written by J.S., C.G., J.P. and R.M.C. All authors read and approved the final manuscript.

Funding Open Access funding enabled and organized by Projekt DEAL.

Data Availability The data utilized in this study are archived at DLR and can be made available upon request.

Declarations

Conflict of interest The authors declare no conflict of interest.

References

Agrawal GP (2010) Fiber-optic communication systems. Wiley, New York. https://doi.org/10.1002/9780470918524

Andrews LC, Phillips RL (2005) Laser beam propagation through random media. SPIE Press, Bellingham

Betz JW (2001) Binary offset carrier modulations for radionavigation. Navigation 48(4):227–246. https://doi.org/10.1002/j.2161-4296.2001.tb00247.x

Costas JP (1956) Synchronous communications. Proc IRE 44(12):1713–1718. https://doi.org/10.1109/JRPROC.1956.275063

Giorgetta FR, Swann WC, Sinclair LC et al (2013) Optical two-way time and frequency transfer over free space. Nat Photonics 7(6):434. https://doi.org/10.1038/nphoton.2013.69

Giorgi G, Schmidt T, Trainotti C et al (2019) Advanced technologies for satellite navigation and geodesy. Adv Space Res. https://doi.org/10.1016/j.asr.2019.06.010

Günther C (2018a) Kepler–satellite navigation without clocks and ground infrastructure. In: Proceedings of the 33rd international technical meeting of the satellite division of the institute of navigation (ION GNSS+ 2018). https://doi.org/10.33012/2018.15997

Günther C (2018b) Kepler– satellite navigation system description and validation. In: Proceedings of the 9th workshop on satellite navigation technologies (NAVITEC 2018). https://elib.dlr.de/126622/

Hauschildt H, le Gallou N, Mezzasoma S et al (2019) Global quasi-real-time-services back to Europe: Edrs global. In: International conference on space optics ICSO 2018. SPIE, pp 353–357

Heine F, M hlnikel G, Zech H et al (2014) The European data relay system, high speed laser based data links. In: 7th advanced satellite multimedia systems conference and the 13th signal processing for space communications workshop (ASMS/SPSC). https://doi.org/10.1109/ASMS-SPSC.2014.6934556

Kaplan E, Hegarty C (2005) Understanding GPS principles and applications. Artech House, Boston

Lipiński M, Włostowski T, Serrano J et al (2011) White rabbit: a PTP application for robust sub-nanosecond synchronization. In: 2011 IEEE international symposium on precision clock synchronization for measurement, control and communication. IEEE, pp 25–30. https://doi.org/10.1109/ISPCS.2011.6070148

Michalak G, Neumayer KH, König R (2020) Precise orbit determination of the Kepler navigation system-a simulation study. In: 2020 European navigation conference (ENC). IEEE, pp 1–10

Michalak G, Glaser S, Neumayer K et al (2021) Precise orbit and Earth parameter determination supported by LEO satellites, inter-satellite links and synchronized clocks of a future GNSS. Adv Space Res 68(12):4753–4782. https://doi.org/10.1016/j.asr.2021.03.008

Poliak J, Mata Calvo R, Surof J et al (2018) Laboratory demonstrator of optical inter-satellite links for the Kepler system. In: Proceedings of the 33rd international technical meeting of the satellite division of the institute of navigation (ION GNSS+ 2018). https://doi.org/10.33012/2018.15886

Seimetz M (2009) High-order modulation for optical fiber transmission, vol 143. Springer. https://doi.org/10.1007/978-3-540-93771-5

Surof J, Poliak J, Mata Calvo R (2017) Demonstration of intradyne BPSK optical free-space transmission in representative atmospheric turbulence conditions for geostationary uplink channel. Opt Lett 42(11):2173–2176. https://doi.org/10.1364/OL.42.002173

Trainotti C, Dassié M, Giorgi G et al (2022) Autonomous satellite system synchronization schemes via optical two-way time transfer and distributed composite clock. In: Proceedings of the 35th international technical meeting of the satellite division of the institute of navigation (ION GNSS+ 2022), pp 3646–3661. https://doi.org/10.33012/2022.18296

Wayne D, Rahimzadeh S, Cote N et al (2024) Connecting the warfighter with lasers in space: the space development agency and the optical communications terminal standard. In: Free-space laser communications, vol XXXVI. SPIE, pp 266–273. https://doi.org/10.1117/12.3005520

Wolf R, Surof J, Poliak J et al (2020) Communication and ranging system for the Kepler laboratory demonstration. In: Proceedings of the 33rd international technical meeting of the satellite division of the institute of navigation (ION GNSS+ 2020), pp 1200–1208. https://doi.org/10.33012/2020.17615

Zhou Y, Wang Y, Huang W et al (2018) In-orbit performance assessment of BeiDou intersatellite link ranging. GPS Solut 22:1–10. https://doi.org/10.1007/s10291-018-0784-0